Astron. Astrophys. 293, 225–239 (1995)

ASTRONOMY AND ASTROPHYSICS

Infrared lines as probes of solar magnetic features

VIII. Mg I 12 μm diagnostics of sunspots

J.H.M.J. Bruls[1,⋆], S.K. Solanki[1], R.J. Rutten[2], and M. Carlsson[3]

[1] Institut für Astronomie, ETH-Zentrum, CH-8092 Zürich, Switzerland
[2] Sterrekundig Instituut, Postbus 80 000, NL-3508 TA Utrecht, The Netherlands
[3] Institute of Theoretical Astrophysics, P.O. Box 1029, Blindern, N-0315 Oslo, Norway

Received 26 July 1993 / Accepted 9 May 1994

Abstract. Due to their large Zeeman sensitivity, the Mg I lines at 12 μm are important diagnostics of solar magnetism. The formation of their central emission features is now understood, enabling quantitative modeling and diagnostic application of these lines. We supply the first systematic analysis of solar Mg I 12 μm Stokes profiles employing detailed line-profile synthesis. We compute Stokes profiles of Mg I 12.32 μm for the quiet Sun, for sunspot penumbrae and for the extended ("superpenumbral") magnetic canopies surrounding sunspots. We use these computations to analyze recent Mg I 12 μm observations by Hewagama et al. (1993).

Our results are the following: (1)—Saha-Boltzmann temperature sensitivity explains that the emission peaks are stronger in penumbrae than in the quiet Sun, and that they disappear in umbrae. (2)—The formation heights of the emission features are approximately the same in penumbrae and in the quiet Sun, namely $\tau_{500} \approx 10^{-3}$. (3)—The simple Seares formula allows relatively accurate determinations of field strength and magnetic inclination. (4)—The observed excess broadening of the σ-component peaks compared with the π component in penumbrae is well explained by primarily horizontal, smooth radial variation of the magnetic field strength. Additional small-scale variations are less than $\Delta B \approx 200$ G. (5)—The vertical field gradients $\partial B/\partial z$ in penumbrae range from 0.7 G km^{-1} to 3 G km^{-1}; the larger gradients occur near the umbra, the smaller ones near the outer edge of the penumbra. (6)—The Mg I 12 μm lines are well-suited to measure the base heights of superpenumbral magnetic canopies. These heights range between 300 km and 500 km above $\tau_{500} = 1$ out to twice the sunspot radius, in excellent agreement with determinations from other infrared lines.

Key words: Sun: magnetic fields – Sun: sunspots

Send offprint requests to: S.K. Solanki
⋆ *Present address:* Instituto de Astrofisica de Canarias, Via Lácteas/n, E-38200 La Laguna, Tenerife, Spain

1. Introduction

The Mg I 12.22 and 12.32 μm (818.06 and 811.58 cm^{-1}) lines appear in the solar spectrum as narrow emission peaks superposed on shallow, wide absorption troughs. The very first study of these Mg I 12 μm lines by Brault & Noyes (1983) already demonstrated their large potential as solar Zeeman diagnostics, since the emission peaks are clearly split for magnetic field strengths down to a few hundred Gauss. Brault & Noyes found that the lines are fully split into separate Zeeman σ components for sunspot penumbrae. For plage regions the Zeeman components are incompletely separated. The lines are not seen in umbrae. The total emission is larger in penumbrae than in the quiet Sun, while it is weaker in plages. Subsequent observations have confirmed these findings, and established the promise of these lines for investigating solar magnetism (Deming et al. 1988, 1991, Zirin & Popp 1989, Hewagama et al. 1993).

The formation of the Mg I 12 μm emission peaks was long a puzzle (e.g. Lemke & Holweger 1987), but recently the peaks have been explained as being due to NLTE (non local thermodynamic equilibrium) line source function enhancement in the upper photosphere (Carlsson et al. 1990, Chang et al. 1991, Carlsson et al. 1992a; cf. Carlsson et al. 1992b, Rutten & Carlsson 1993). These studies have opened the way for detailed spectral synthesis of the Mg I 12 μm lines from magnetic structures in the solar photosphere. This is the theme of the present paper. It is the first analysis applying detailed NLTE line-formation modeling to observations of the 12.32 μm line from magnetic structures.

We expand the quiet-Sun analysis of Carlsson et al. (1992a) and the simple computation of Mg I 12 μm Zeeman profiles of Rutten & Carlsson (1993) by synthesizing Stokes I, Q, U and V profiles of the Mg I 12.32 μm line from sunspot penumbrae as well as from the superpenumbral magnetic "canopies" which surround sunspots. Because the emission peaks of the Mg I 12 μm lines map NLTE source function structure in a optically thick manner and because the Zeeman encoding of these lines depends on the magnetic field geometry and on the atmo-

spheric stratifications inside and outside the magnetic structures, detailed NLTE synthesis of Stokes profiles appears to us to be the safest approach. These dependences mix together in complicated fashion; only numerical modeling can disentangle them. We employ such computations here to investigate the magnetic and thermodynamic sensitivities of the Mg I 12.32 μm line, and we also try to reproduce various properties of these lines that are observed in and around sunspots. Our goal is to learn more about sunspots as well as about the Mg I 12 μm lines.

The observed Mg I 12 μm profiles indicate the presence of a range of magnetic field strengths in the atmospheric layers where the emission peaks are formed, because the central peaks (π component and non-magnetic contribution) are observed to be narrower at disk center than the σ component peaks. The central peak has a FWHM (full width at half maximum) of 17 milliKayser (1 mK $\equiv$ 10^{-3} cm^{-1}) for the quiet Sun and 14 mK FWHM for penumbrae (Brault & Noyes 1983), whereas the σ components show 22 mK FWHM in spectra from plages and penumbrae (Deming et al. 1988; Hewagama et al. 1993). Deming et al. (1988) used an optically-thin formation estimate to conclude that this excess σ-peak broadening cannot be explained by smooth outward decay of the magnetic field strength across sunspot penumbrae. We employ detailed line-formation computations to address this issue (finding the opposite), and also to determine the size of vertical gradients in penumbral field strengths.

We also study the field configuration outside sunspots, i.e. the way in which magnetic fields fan out from a sunspot to form a "magnetic canopy" with field-free plasma underneath. The Mg I 12 μm emission features provide suitable diagnostics to study such canopies, because they are formed in the upper photosphere (Carlsson et al. 1992a), at just the heights expected for the base of such superpenumbral canopies (Giovanelli 1980; Giovanelli & Jones 1982; Solanki et al. 1992, 1993). Indeed, Hewagama (1991) and Hewagama et al. (1993) report Mg I 12 μm measurements of almost horizontal magnetic fields of considerable strength around penumbrae, which we re-interprete here as due to canopies.

In Sect. 2 we specify our model atom, model atmospheres, and computational method. We then discuss Mg I 12 μm line formation in Sects. 3 and 4 for the non-magnetic solar atmosphere, first comparing our computations with the results of Carlsson et al. (1992a) and then computing Mg I 12 μm profiles for a grid of model atmospheres which differ in temperature stratification, in order to discuss the formation heights and the emission strengths of the Mg I 12 μm lines for different conditions. We then proceed to re-analyze data from Hewagama et al. (1993) on the basis of our detailed line-synthesis computations. In Sects. 5 and 6 we model Stokes profiles and the widths and asymmetries of the emergent Zeeman components; in Sect. 7 we discuss vertical field gradients within penumbrae, and in Sect. 8 we constrain the height of superpenumbral canopies. We end the paper with conclusions in Sect. 9.

2. Input data and methods

2.1. Model atom

The atomic data for this analysis are the same as employed by Carlsson et al. (1992a). These are, per level or transition, probably not definitive, especially as regards collision cross-sections, but they have the important advantage of homogeneity throughout the Mg I Grotrian diagram. Such internal consistency is important because the regularity of the patterns in the bound-bound and bound-free cross-section matrices is crucial to the formation of the Mg I 12 μm emission features. In setting up the model atom for this study (at Zürich rather than Oslo), we found various mistakes (in oscillator strengths of lines to and from ^{1}F^o) that are corrected in the present modeling. These corrections change the results somewhat, but less than the uncertainties present in the atomic data already. The results of Carlsson et al. (1992a) are recovered by changing the forbidden collisional strengths to 30 % of the value for the closest allowed transition. Larger differences result from the different treatment of ionizing radiation fields, discussed in Sect. 2.3 below.

Both the Mg I 12.2207 and 12.3183 μm lines are composite, consisting of triplet and singlet components which nearly coincide in wavelength. All components are well within the Doppler widths of the individual lines, since the fine structure splitting within the terms is very small, only a few mK in L-S coupling (Chang 1987; Hewagama 1991), and because also the singlet and triplet terms fall together. Although pertinent data are not available for the singlet and triplet strength ratio, analogy with Mg I transitions at lower excitation energy suggests that the singlet is much weaker and may safely be neglected.

The small fine structure splitting implies that the Mg I 12 μm lines are in the Paschen-Back regime for the magnetic field strengths characteristic of sunspots (Chang 1987). Hewagama (1991) evaluated the splitting pattern (reproduced in a different representation in Fig. 1) and concluded that for field strengths above a few hundred G it only adds field-independent broadening of up to 1 mK to an otherwise normal Zeeman triplet with Landé factor $g_{\rm eff}$ = 1. The effective Landé factor of the 12.32 μm line was experimentally found to be $g_{\rm eff}$ = 0.992 for field strengths between 200 and 800 G by Lemoine et al. (1988). Thus, for field strengths that are characteristic of solar plage regions and (pen)umbrae, normal Zeeman splitting with $g_{\rm eff}$ = 1 may readily be applied. Note that the Paschen-Back effect can lead to asymmetries between the two σ components even in the absence of velocities (Mathys 1990; cf. Sect. 6 below).

2.2. Atmospheric models

The atmospheric models used in this analysis are a grid of line-blanketed radiative equilibrium (RE) models with different temperature stratifications (see Fig. 3), taken from Kurucz (1991) and parametrized by their effective temperatures $T_{\rm eff}$ which range from 3500 K to 6000 K. In addition, we use the comparable RE model T5780 from Uppsala (Edvardsson et al. 1993), which was also employed by Carlsson et al. (1992a). These models formally are flux constant models, since a mixing-

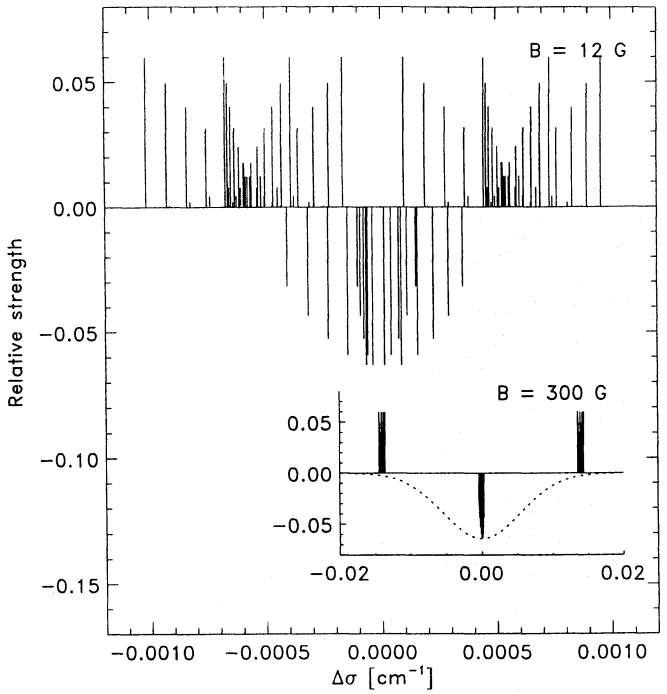

Fig. 1. Splitting pattern of the Mg I 12.32μm line. The total strength of the combined σ- and π-components has been normalized to unity; the fine structure constituents of the π component are drawn negatively. In order to display detail, the splitting pattern is shown here for a magnetic field strength of only 12 G, although that is outside the Paschen-Back regime, so that the fine structure splitting can no longer be treated as a perturbation on normal Zeeman triplet splitting. At this field strength, the two forests of σ-peaks are just separated. The more pertinent splitting pattern for a 300 G magnetic field (inset) illustrates that the broadening of the three classical Zeeman triplet components due to atomic fine structure splitting is negligible. The dotted curve is a Gaussian profile representing 2 km s^{-1} thermal Doppler broadening, which corresponds to T = 5880 K (arbitrary ordinate scale)

length convection treatment was used in generating them, but the radiative equilibrium criterion is satisfied at the 12.32 μm line formation heights. The microturbulence value of the Kurucz models has been decreased from 2.0 km s^{-1} to 1.0 km s^{-1} in order to suit solar conditions. None of these models possesses a chromospheric temperature rise; nevertheless, they produce Mg I 12 μm emission features because these are due to NLTE processes in the photosphere. The RE atmospheres T4000 (i.e. $T_{\rm eff}$ = 4000 K) and T5000 are used below as umbra and penumbra models, respectively. The Kurucz T5750 model closely resembles the Uppsala T5780 model which is taken to represent the spatially-averaged quiet Sun. In addition, we use various magnetic field configurations for test purposes. Only a few of them are representative of real solar magnetic structures.

2.3. Radiative transfer computations

The statistical equilibrium and radiative transfer equations are solved for each of the non-magnetic atmospheres listed above, employing version 2.0 of Carlsson's (1986) MULTI code and using its local operator option (cf. Olson et al. 1986). The computed line source functions and opacities are then used as input for the Diagonal Element Lambda Operator (DELO) Stokes profile synthesis code (Rees et al. 1989; Murphy & Rees 1990; Murphy 1990), which evaluates magnetically split line profiles for any magnetic field configuration and line of sight. We so assume that the presence of magnetic field does not influence the statistical equilibrium populations. This is the so-called field-free approximation which has been shown to introduce little error into the computed line profiles (e.g. Rees 1969; cf. Rees 1987).

The original opacity package of MULTI (version 1.0), which dates back to LINEAR (Auer et al. 1972), has been modified for this analysis in two respects. First, more recent neutral-metal photoionization cross-sections have been taken from Mathisen (1984). Second, wavelength-dependent fudge factors are applied to the opacities in order to simulate the ultraviolet "line haze" constituted by the millions of spectral lines in that wavelength region. These fudge factors have been determined empirically by trying to reproduce the observed disk-center continuum of the quiet Sun (cf. Bruls 1992), i.e. by reproducing a smooth curve through the highest points in the spectrum. This procedure ignores the presence of the numerous strong lines which depress the wavelength-averaged intensity appreciably. Consequently, the ultraviolet continua computed here overestimate the actual amount of radiation. The main effect is to produce larger Mg I overionization, especially in the $3s3p\,^3P^0$ bound-free edge at 251 nm. This ionization rate influences the amount of emission in the 12 μm cores, because it adds to the photon losses in infrared lines in driving the establishment of a recombination flow along the Rydberg levels to which the 12 μm lines belong (cf. Carlsson et al. 1992a, Rutten & Carlsson 1993). Too much radiation in the $3s3p\,^3P^0$ ionization edge therefore causes too large emisssion in the 12 μm lines.

Simply including additional line opacity, however, is not a straightforward option. One should not only add line haze opacities but must also prescribe line haze source functions. Since most strong lines above λ = 200 nm do not show central emission peaks, NLTE scattering clearly affects their formation. In addition, interlocking by optical pumping is observed to take place at these wavelengths (Canfield et al. 1978), while the strongest lines have frequency-dependent source functions due to partial redistribution (e.g. Canfield & Cram 1977).

Thus, short of full-fledged NLTE line-haze computation (cf. Anderson 1985, 1989, 1991), one needs to resort to tractability assumptions. In the Mg I modeling of Chang et al. (1991) the source function for the opacity-sampled line haze is arbitrarily set to transit from LTE to full scattering in the upper photosphere, so that the lines do not respond to the chromospheric temperature rise. The modeling of Carlsson et al. (1992a) relies on the ultraviolet radiation fields computed with the T5780 atmosphere, which are based on opacity sampling with 0.07 nm spacing and LTE source functions in the absence of a chromosphere and should be accurate below the temperature minimum. These choices probably contribute to the differences between the Mg I modeling of Chang et al. (1991) and of Carlsson et al.

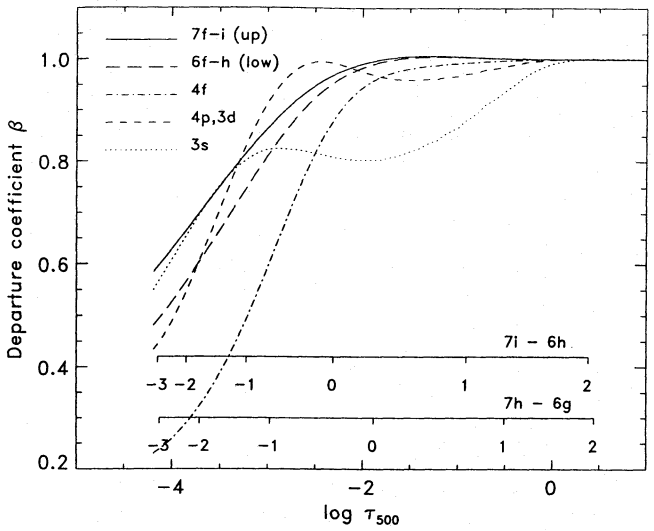

Fig. 2. Population departure coefficients β for the quiet-Sun model T5780 (RE, $T_{\rm eff}$ = 5780 K). The $7f$–i curves (solid) represent the upper levels of the 12 μm lines, the $6f$–h curves (long dashes) their lower levels; $3s$ is the ground state, $3d$–$4f$ are representative low-excitation levels. The abscissa measures continuum optical depth at λ = 500 nm. The two inset optical depth scales are for the centers of the 12.32 μm line ($7i$–$6h$) and the 12.22 μm line ($7h$–$6g$), respectively. The outward divergence between the solid and dashed curves causes the emission features in these two lines

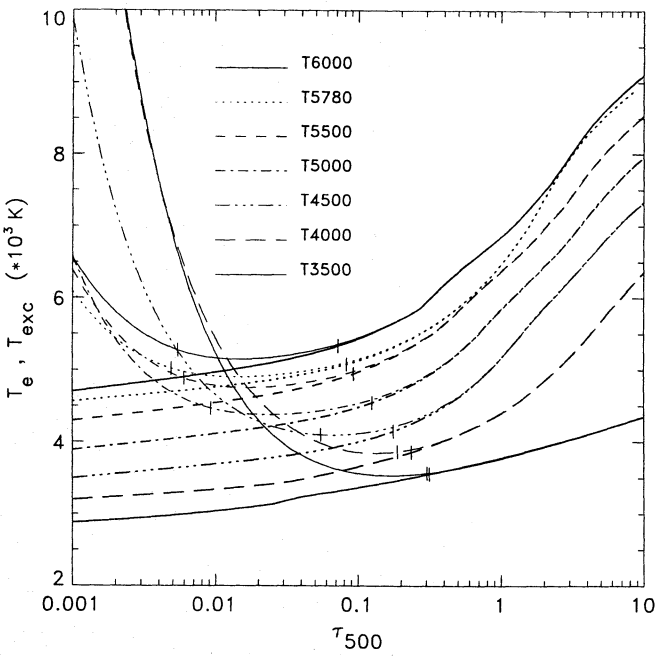

Fig. 3. Electron temperatures $T_{\rm e}$ (curves that decrease monotonically outward) and excitation temperatures $T_{\rm exc}$ for RE models with different $T_{\rm eff}$ against the continuum optical depth at 500 nm. The dotted curves are for the Uppsala T5780 model which represents the quiet Sun. The tickmarks indicate unity optical depth for the 12 μm continuum (on the $T_{\rm e}$ curves) and for 12.32 μm line center (on the $T_{\rm exc}$ curves)

(1992a) and Rutten & Carlsson (1993), and also to the differences between the modeling of comparable infrared H I lines by Carlsson & Rutten (1992, 1993) and by Avrett et al. (1993) (cf. Rutten & Carlsson 1993).

Since detailed theoretical radiation fields were not available for the models with lower effective temperature used here, we have elected not to add additional ultraviolet line opacity to our continuum fudging. Obviously, our Mg I line profiles are sensitive to this choice, or to any other treatment of the ultraviolet line haze. In addition, the opacity fudge factors used here are derived for quiet-Sun models employing spatially-averaged solar data; they may not apply to the other models which we employ to describe magnetic fine structure. These uncertainties keep us from detailed fitting of observed line profiles in this paper; instead, we concentrate on demonstrating characteristics of Mg I 12 μm line formation with differential experiments that at least offer internal consistency. Our conclusions below therefore should not be depend strongly on the line-haze treatment.

3. Quiet-Sun NLTE departures

Figure 2 shows results for model T5780 in the form of NLTE population departure coefficients β, defined as the ratio of the actual NLTE population and the LTE Saha-Boltzmann population $\beta_{\rm i} = n_{\rm i}/n_{\rm i}^{\rm LTE}$ (cf. Wijbenga & Zwaan 1972). Comparison with Fig. 9 of Carlsson et al. (1992a), who used the same model atmosphere and nearly the same model atom, shows slight differences which are primarily due to the differences in angle-averaged ultraviolet radiation fields discussed above. Our computation results in slightly larger overionization and correspondingly larger depression of the β coefficients below unity. The divergence between the curves for levels $7f$–i and $6f$–h is also slightly larger, because the increased photoionization also helps driving a larger recombination flow through the Rydberg levels.

The effect of the departures and their divergence on the 12.32. μm line is shown by the T5780 curves (dotted) in Fig. 3. The divergence causes the outward upturn of the line source function, plotted here in the form of excitation temperature $T_{\rm exc}$. It is steep even for slight divergence due to the influence of stimulated emission in the infrared (Lemke & Holweger 1987, Carlsson et al. 1992a). The divergence also affects the line opacity, but this effect is smaller. The tick on the $T_{\rm exc}$ curve specifies the line-center optical depth unity location.

Compared to the modeling of Carlsson et al. (1992a) the NLTE line source function rises more steeply, but the line is formed slightly deeper due to the smaller opacity. The first effect wins; the emission features are approximately 35% larger in the present computation than in Fig. 6 of Carlsson et al. (1992a).

4. Radiative-equilibrium atmospheres

Figure 3 also displays results for the different RE models from Kurucz, plotting the 12.32 μm line and continuum source functions (the latter are equal to the Planck function), in the form of excitation temperature $T_{\rm exc}$ and electron temperatures $T_{\rm e}$, against the corresponding continuum optical depth scale at λ = 500 nm. This plot shows that the line is formed in very

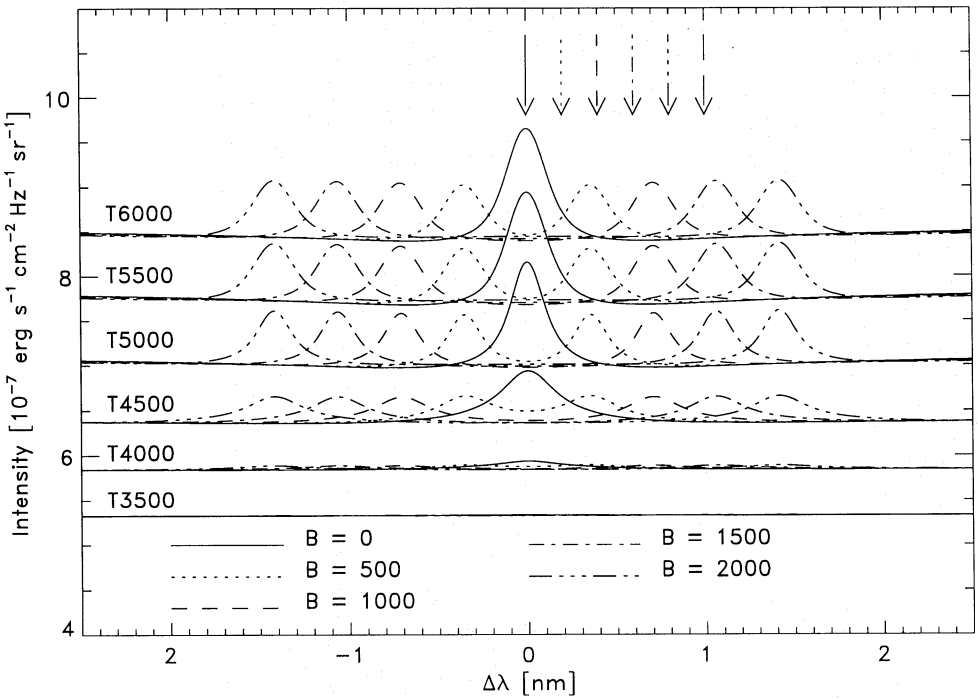

Fig. 4. Disk-center Mg I 12.32 μm profiles for RE atmospheres with different $T_{\rm eff}$ (specified at left) and for different longitudinal field strengths B (specified by line coding). All intensities are plotted on a single absolute scale. The coded vertical arrows at the top mark the wavelengths of the contribution functions in Fig. 5. The relative line emission is largest for $T_{\rm eff} \approx 5000$ K

deep layers for the cooler models, barely above the continuum formation height. For the hotter models there is little variation in formation height; the line-center ticks lie around $\tau_{500} \approx 0.006$ for $T_{\rm eff} \geq 5000$ K.

Figure 4 shows resulting Mg I 12.32 μm profiles. The relative emission (peak height over the continuum) reaches a maximum of 15% above the continuum for $T_{\rm eff} = 5000$ K and disappears below $T_{\rm eff} = 4000$ K. The absorption troughs are present but not prominent due to the scaling of the axes.

The peak amplitude behavior is set by Saha-Boltzmann statistics, from which the Mg I Rydberg populations differ only slightly at the heights of 12 μm line formation since their departure coefficients β are close to unity (Fig. 2). At the lower temperatures, the populations of the high-excitation levels decrease strongly with the Boltzmann factor; at the higher temperatures, their populations decrease again because magnesium is increasingly ionized. This temperature sensitivity corresponds to the observed properties of the 12.32 μm line. It is stronger in penumbrae (here characterized by model T5000) than in the quiet Sun ($T_{\rm eff} = 5780$ K), and it is not observed in umbrae ($T_{\rm eff} \approx 4000$ K). Thus, simple Saha-Boltzmann population statistics explain the observed differences in behavior between different solar regimes, just as for the differences between Rydberg line strengths of Mg I, H I and other neutral species in the solar infrared (Carlsson et al. 1992a).

When longitudinal magnetic fields are present at constant strength, the emission is equally divided over the two σ-peaks, without a π component. This is shown as function of field strength by the non-solid profiles in Fig. 4, for which peak height is independent of field strength (cf. Rutten & Carlsson 1993). The σ-peaks are well separated at $B = 500$ G.

We estimate magnetic line formation depths from line depression contribution functions $C_{\rm R,X}$, with $X = I, Q, U, V$ designating the Stokes vector components (cf. Magain 1986; Grossmann-Doerth et al. 1988). These contribution functions are normalized so that $\int C_{\rm R,X}(\nu)\, {\rm d}\log\tau_{500} = D_{\rm X}(\nu)$, where $D_{\rm X}(\nu)$ is the relative line depression and τ_{500} the optical depth in the 500 nm continuum. Note that negative line depression implies emission; we therefore plot the $C_{\rm R,X}$ upside down, as is done in the comparable contribution function plots of Carlsson et al. (1992a) and Rutten & Carlsson (1993).

Figure 5 displays Stokes I line emission contribution functions $-C_{\rm R,I}$ for different RE models and for three values of the longitudinal field strength B (disk center, vertical, height-independent field). These are plotted for various representative wavelengths in the line, indicated by the arrows at the top of Fig. 4. The positive parts of $-C_{\rm R,I}$, high in the atmosphere, show the contribution to the emission; the negative parts in the deeper atmosphere represent the underlying absorption trough. For example, the T5500 panel in the top row ($B = 0$ G) shows the contribution to the quiet-Sun like emission peak as a wide hump in the line-center curve (solid) around $\log\tau_{500} = -3.2$, and the contribution to the absorption trough as dips in the line-wing curves around $\log\tau_{500} = -1.5$.

The absorption contribution dips reach about the same amplitude in all panels. The emission humps are roughly halved in amplitude when magnetic field is present (lower panels), because they then specify the contributions to the right-hand

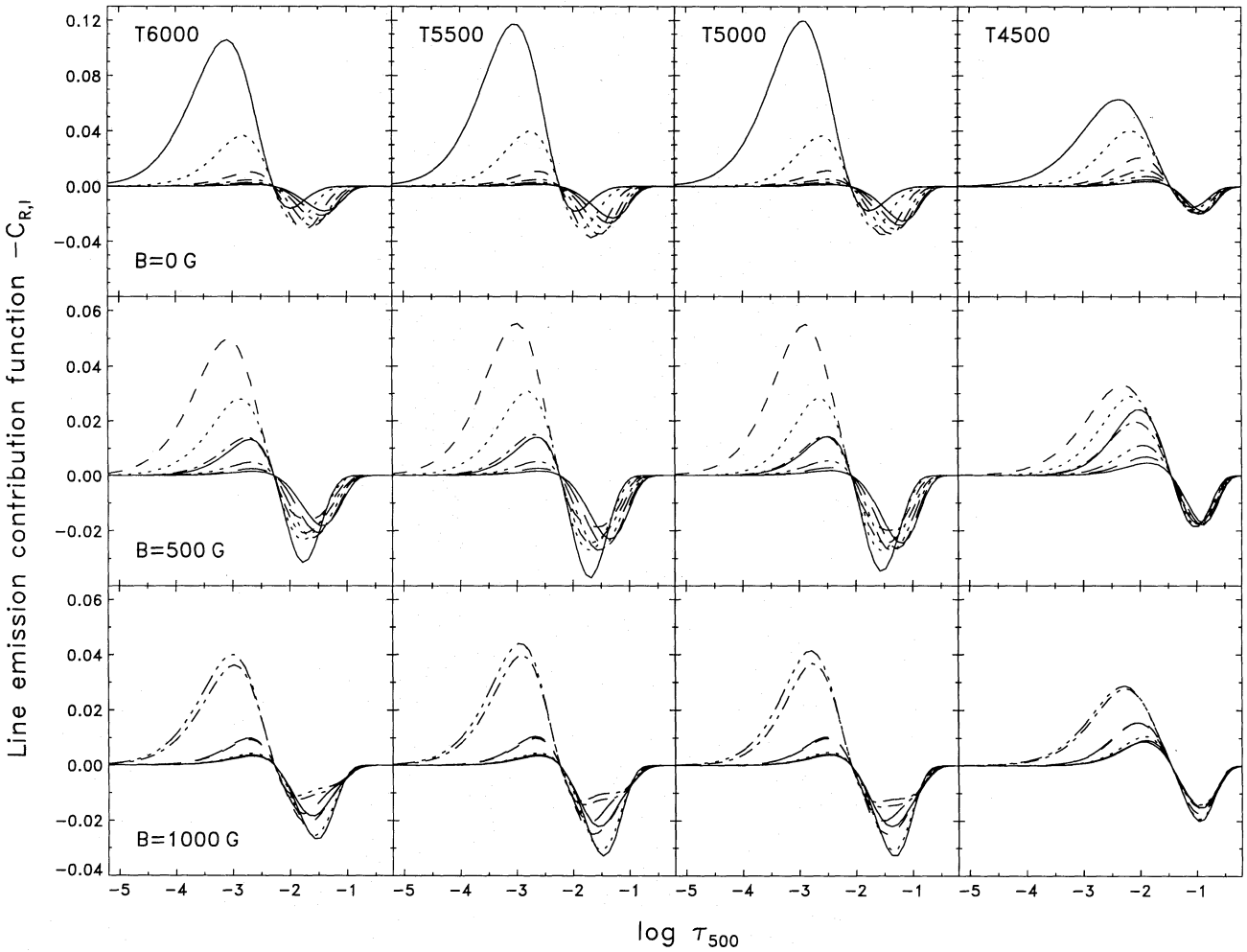

Fig. 5. Line emission contribution functions to Stokes I, defined here as the negative line depression contribution functions $-C_{R,I}$, for the radiative equilibrium (RE) models indicated at the top of the columns. The rows are for longitudinal magnetic fields with strengths B = 0, 500 and 1000 G. $C_{R,I}$ is plotted for the wavelengths indicated by arrows in Fig. 4, respectively at 0 (solid), 0.2 (dotted), 0.4 (dashed), 0.6 (dot-dashed), 0.8 (triple dot-dashed), and 1.0 nm (long dashed) from line center; these wavelength samples cover the whole line profile. Note the scale change between the upper row and the two lower rows

σ component only, at the wavelength offsets shown in Fig. 4. They curves are also nearly equal to the Stokes V contribution functions for $B > 200$ G. The location of the deepest dip is about the same in all panels. The central emission peak for $B = 0$ and the σ components for $B \neq 0$ are all formed roughly between $\log \tau_{500} = -4.5$ and -2.0 ($-3.5 \leq \log \tau_{12} \leq -1.0$). A fortunate characteristic of the formation of the σ components is therefore that their formation height does not vary significantly with field strength or temperature, except for $T_{\rm eff} < 5000$ K. Thus, both in quiet areas and in sunspot penumbrae the Mg I 12 μm lines are formed at $\tau_{500} \approx 10^{-3}$.

5. Stokes profiles and Zeeman sensitivity

Figure 6 displays Stokes vector profiles (all four components) for a more complex magnetic field configuration with field strength $B = 2000$ G, inclination angle $\gamma = 45°$ and azimuth angle $\chi = 15°$ (for definitions see e.g. Rees 1987). The unpolarized Stokes I profile shows an unshifted π component and two displaced, fully separated σ components. The latter are superposed on the shallow absorption trough, which is due to the very wide Stark-broadened line wings, maps the shallow gradient of the Planck function with height, and is sometimes absent in Mg I 12 μm observations if a narrow filter is used to increase the signal to noise ratio (e.g. Deming et al. 1988).

The Stokes V component shows two fully separated peaks with opposite signs, superposed on wider features which again have opposite signs. The latter represent the Stokes V signature of the absorption trough. They are incompletely separated due to their large widths; therefore, the amplitude of their Stokes V signal is still proportional to B. The Stokes Q and U components primarily show the emission parts. The signal from the trough is still in the quadratic regime and therefore smaller than in Stokes V.

Some studies employing the 12 μm lines are restricted to determining the magnetic field strength B from the wavelength

separation of the σ-component maxima in Stokes I (e.g. Brault & Noyes 1983, Zirin & Popp 1989); similarly, one may measure the Stokes V peak separation. We test this simple procedure in Fig. 7. Measuring longitudinal fields from Stokes V splitting (curves above the dotted diagonal) is more accurate than measuring transverse fields from Stokes I splitting (curves below diagonal), because Stokes I requires a larger field strength for unambiguous σ component separation due to the disturbing presence of an unshifted central peak, in the form of a π component from transverse fields, and/or of a central peak from non-magnetic plasma within the resolution element. Figure 7 indicates that V-splitting measurement is reliable for $B \geq 200$ G while I-splitting is only reliable for $B \geq 500$ G, with a slight dependence on temperature in the sense that larger magnetic field strengths are required to achieve sufficient splitting at lower temperatures (dashed). The next step in sophistication, namely the fit to the observed profiles with a set of Gaussians or similar functions (e.g. Hewagama et al. 1993) should significantly enhance the sensitivity to the field and the accuracy of the measured fields. In this sense Fig. 7 shows the largest possible errors in the field strength obtained from the 12μm lines (for ideal profiles).

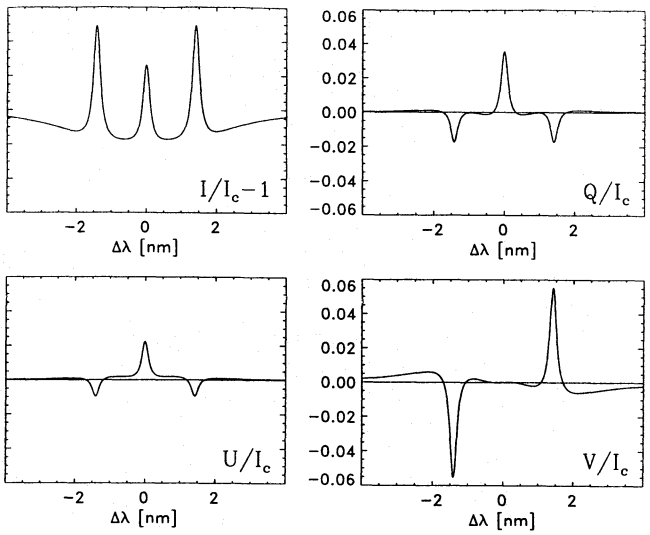

Fig. 6. Stokes vector profiles for magnetic field configuration with strength B = 2000 G, inclination angle γ = 45°, azimuth angle χ = 15°. The ordinate scales are the same for all panels, in units relative to the continuum intensity I_c

The inclination and azimuth angles γ and χ of the magnetic vector may be estimated directly from observed ratios of the σ and π components in Stokes I, Q, U and V (Hewagama et al. 1993). For completely split profiles use of the Seares' (1913) equations may deliver these angles without detailed profile modeling. However, it is unclear how important the treatment of the absorption trough is, or whether it is possible to reliably determine the vector magnetic field from the observed σ- and π-intensity ratios of Stokes I alone (cf. Deming et al. 1988), since stray light, although much less of a problem in the thermal infrared than in the visible, distorts the observed Stokes I profiles by an unknown amount. Furthermore, the Seares' equations are valid only for optically-thin lines formed in uniform magnetic fields, whereas the Mg I 12 μm lines are not optically thin (Carlsson et al. 1992a), and the magnetic fields of solar penumbrae, plage and quiet areas are far from uniform.

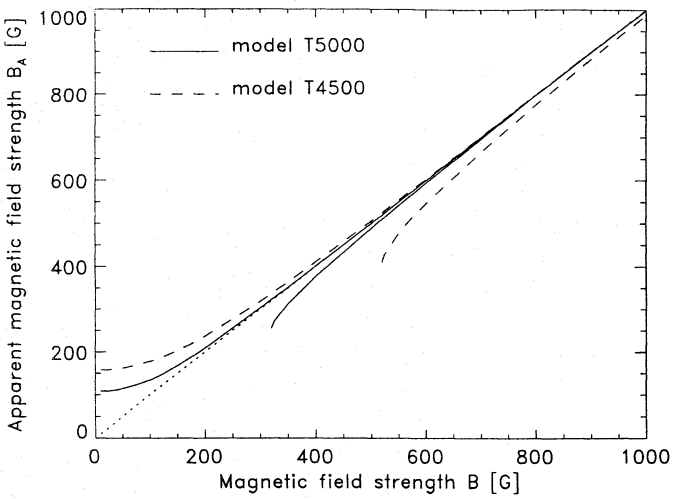

Fig. 7. Calibration of magnetic field measurements from line profile splitting, for RE models T4500 and T5000 and for Stokes V and I. The curves above the diagonal represent the apparent longitudinal magnetic field strength B_A that would follow from measurement of the separation of the σ components in Stokes V profiles due to actual longitudinal fields of strength B. The curves below the diagonal are similar calibrations for measuring transverse fields from Stokes I splitting due to actual transverse fields of strength B. The latter curves are not shown for field strengths which do not produce discerneable σ-features in Stokes I profiles due to overlap with the central π component; they deviate more from the diagonal than the upper curves for the same reason. Measuring Stokes I splitting from actual longitudinal fields would correspond to the upper Stokes V curves only when no non-magnetic plasma is present; the lower curves represent a more realistic case

Therefore we show in Fig. 8 a test of the validity of the Seares approximation for the determination of the field inclination angle γ from Stokes I for the simple case of a height-independent field and no stray light. The intensities of the σ- and π-components required to form the intensity ratios are measured from the minimum in each line profile. Three different field strengths are considered: B = 500, 1000, and 2000 G. Figure 8 shows that the Seares formulae recover the magnetic inclination surprisingly well for the higher field strengths. For B = 500 G and $\gamma \approx 0$ or $\gamma \approx 90°$ the accuracy is somewhat lower. Difficulties will arise with this procedure when the magnetic filling factor deviates from unity. When more Stokes components are taken into account lower errors can be obtained. Profile fitting, such as carried out by Hewagama et al. (1993), should also increase the accuracy. Thus, again, Fig. 8 represents a worst case.

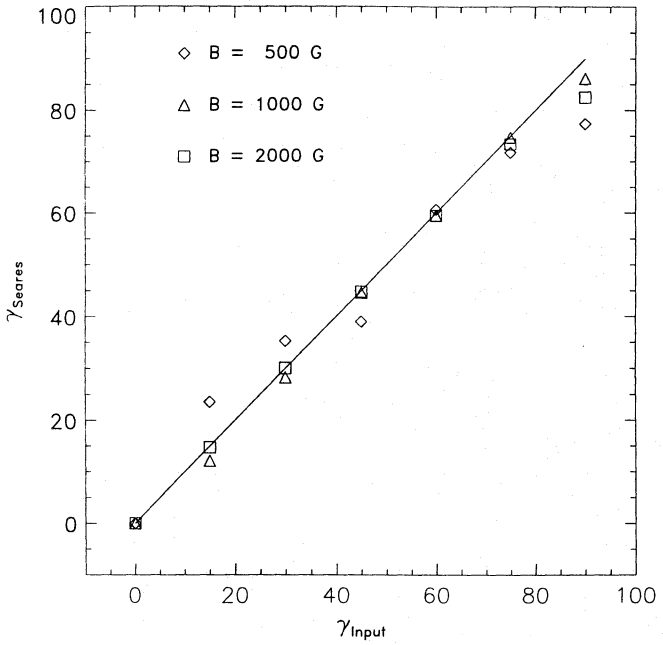

Fig. 8. Seares' approximation for determining field inclination γ applied to three different cases: height-independent field strength B = 500 (diamonds), 1000 (triangles) and 2000 Gauss (squares). In each case the field azimuth is taken to be $\chi = 15°$. The exact result is the diagonal line

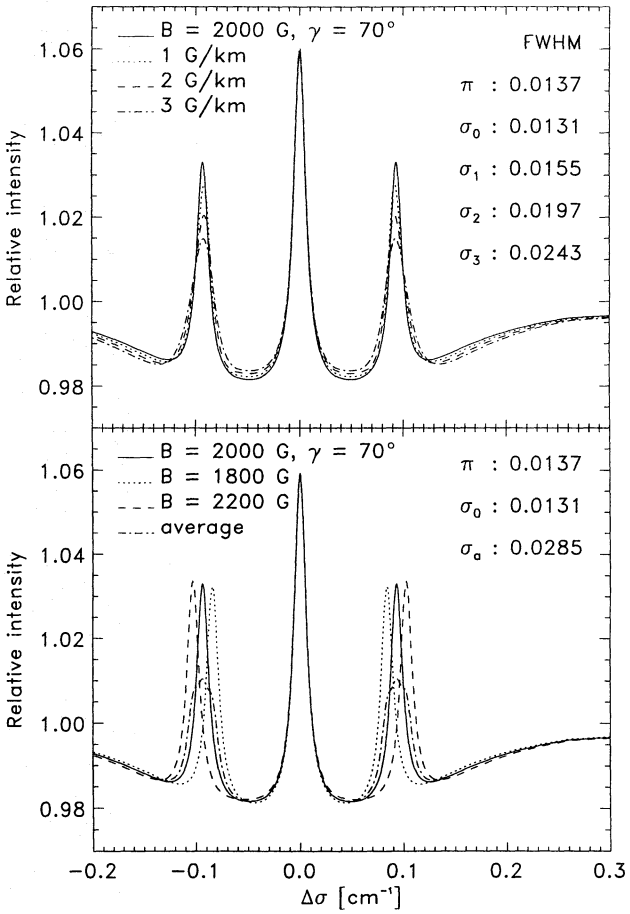

Fig. 9. Stokes I profiles for RE model T5000, which characterizes solar penumbrae, and inclined magnetic fields with $\gamma = 70°$. The halfwidths of the peaks are specified in cm^{-1} at right in each panel. *Upper panel:* 12.32 μm line profiles for uniform magnetic field (solid) and for vertical gradients $\partial B/\partial z$ of 1, 2 and 3 G km^{-1}, respectively. In each case, B is set to 2000 G at the line formation height h = 450 km above $\tau_{500} = 1$. *Lower panel:* 12.32 μm line profiles for uniform fields at the three specified strengths, averaged together with equal weights in the "average" profile. Its width σ_a is specified at right

6. Widths and asymmetries of Stokes components

Another important observed property of the Mg I 12 μm profiles which requires modeling by detailed radiative transfer computations is the excess width of the σ components over the π component. The observations of Brault & Noyes (1983) already show, even without polarization analysis, that there are significant differences between the shape of the σ components and the π component. The FWHM of the π component varies only moderately over the solar disk. It is 17 mK at disk center and 21 mK near and just off the solar limb in quiet-Sun data, and it is 14 mK in penumbrae (cf. Hewagama et al. 1993). Indeed, one would expect the π component to be narrower in penumbrae than in the quiet Sun, because it arises from regions with transverse magnetic fields. Mass flows across field lines should be largely inhibited in those regions, so that any nonthermal motions should also be mainly transverse and produce less penumbral π-component broadening than in the quiet Sun. Thermal broadening is relatively unimportant. Note that the profiles in Fig. 4 are actually wider for lower $T_{\rm eff}$; this increase is due to increased pressure broadening because for cool models the Mg I 12 μm lines are formed deeper, at higher density.

The width and the shape of the σ components vary strongly from one location in the penumbra to another (Hewagama et al. 1993, Fig. 11). The average width is about 22 mK; thus, each σ component is approximately 1.5 times as broad as the π component. The fine-structure splitting of the σ components adds only about 1 mK to their widths (Chang 1987, cf. Fig. 1), so does not cause the excess broadening. To explain the latter by nonthermal motions one needs at least 3 km s^{-1} velocity broadening along the line of sight, within the spatial and temporal resolution of the data. Such large broadening considerably exceeds the actual penumbral velocities observed by Lites et al. (1990) at very high spatial resolution. It is possible that the excess σ-peak broadening is caused by small-scale large-amplitude oscillatory motions that run exclusively along field lines (so do not affect the π component), and exist only in layers above the formation height of the photospheric Fe I 630.25 nm line used by Lites et al. (1990), but the σ-peak asymmetries that are present in Fig. 11 of Hewagama et al. (1993) suggest that the excess broadening is of magnetic origin. In that case, it may be caused by magnetic field inhomogeneities, for example vertical field stratification or horizontal field variations. We test these options here and in the following section,

Figure 9 displays results from 12.32 μm profile computations for different magnetic field strengths. The RE T5000 model is taken to be characteristic of solar penumbrae, with the microturbulent velocity set to zero to reduce the width of the computed π component to the observed value of 14 mK. The upper panel displays the computed line profile for uniform magnetic field strength B = 2000 G with inclination angle $\gamma = 70°$, and also profiles for fields with vertical gradients $\partial B/\partial z$ of 1 – 3 G km^{-1}, respectively. They show that even a gradient of 2 G km^{-1} is insufficient to produce sufficient broadening; the computed FWHM values (specified at right) only reach the observed value of 22 mK for field gradients as large as $\partial B/\partial r$ = 3 G km^{-1}. We find below (Sect. 7) that $\partial B/\partial r$ = 2 G km^{-1} already presents an upper limit to the actual field gradients in most of the penumbra. Thus, although vertical B gradients cannot be rejected as the main σ-component broadening agent, we still need to consider other sources of σ-component broadening.

The lower panel of Fig. 9 displays profiles computed for three different field strengths, as well as the average profile obtained by adding these three profiles together with equal weights. It indicates the amount of broadening which would be produced by horizontal field strength variations within the resolution element. Its halfwidth is 28.5 mK, showing that a 400 G wide distribution already produces σ-peak broadening in excess of most of the widths observed by Deming et al. (1988), in rough agreement with their optically thin estimate that a Gaussian distribution with a width of 470 G would explain these. Computations for a larger set of lines of sight through an actual penumbral model with an assumed field gradient, and convolution of the resulting line profiles with the instrument profile may result in a somewhat different value for the width of the field distribution.

The major question now is to discriminate between smooth large-scale radial variations $\partial B/\partial r$ and the presence of small-scale inhomogeneity in B. The magnitude of the former can be constrained from the angular extent of the entrance apertures used in the observations and from the value of $\partial B/\partial r$ deduced from B measurements at different radial positions in the spot. Deming et al. (1988) used such "sunspot slices" to estimate that the large-scale $\partial B/\partial r$ is insufficient to explain the observed broadening. However, Brault & Noyes (1983) used a larger entrance aperture than Deming et al. (1988) and obtained much broader σ components which indicates large-scale field structuring; moreover, our finding that field variations over only 300–400 G suffice to explain the σ-peak widths observed by Hewagama et al. (1993) agrees roughly with the actual $\partial B/\partial r$ deduced from their spatial slices. Since these values correspond, there isn't much room for other spatial field strength variations than such smooth ones across the field of view. We estimate that small-scale horizontal field inhomogeneity of order ±200 G at the height of formation of the 12 μm lines would already produce too much additional broadening.

Furthermore, we note from the Stokes data in Appendix A of Hewagama (1991) that there is some correlation between the average field strength and the width of the σ components in penumbrae. This suggests that the magnetic field strength distribution becomes slightly wider towards the umbra. Again, this might be due to larger small-scale variations, but these are not observed by Lites et al. 1990 at photospheric levels; a more likely explanation is that the larger-scale gradients $\partial B/\partial r$ and $\partial B/\partial z$ increase closer to the umbra, as predicted by theoretical sunspot models (e.g. Schlüter & Temesvary 1958, Osherovich 1982, Pizzo 1986, Jahn 1989).

Finally, we note that the two σ components are observed to differ in amplitude. The penumbral profiles shown by Brault & Noyes (1983) display a slight amplitude difference, with the blue σ peak larger than the red one; on the other hand, Deming et al. (1988) found opposite asymmetry in some of their observations. Since both data sets were acquired with the Kitt Peak McMath telescope but with different post-focus equipment, it is not likely that this asymmetry is induced by the instrumentation other than the heliostat orientation. The line profiles plotted by Hewagama (1991, Appendix A) tend to show stronger blue than red σ peaks; the occurrence of reverse asymmetry is too rare in his data to search for correlation with other parameters. Thus, the presently available data are not yet suited to detailed modeling of these σ-peak differences. We therefore point out only that they may follow from instrumentally induced crosstalk between Stokes parameters (it should then be largest in Stokes I for large Stokes V values), to the partial Paschen-Back effect (see Mathys 1990), or to the presence of velocity gradients. Note that the latter need not be oriented along the line of sight, because such amplitude asymmetry is produced in Stokes I by the presence of the absorption trough even if the σ components are only shifted relative to the π component, for example by field-aligned motions. However, in order to produce difference between the Stokes V σ components one needs to invoke longitudinal velocity gradients (e.g. Illing et al. 1975, Auer & Heasley 1978, Makita 1986, Solanki & Pahlke 1988, Sánchez Almeida & Lites 1992, cf. Solanki 1993). It will therefore be of great interest to obtain simultaneous observations of Stokes I and V σ-peak amplitudes.

7. Vertical gradients in penumbra fields

In Sect. 6 we have discarded vertical magnetic field gradients as major agent to cause σ peak broadening. The issue in this section is to determine the actual vertical gradients of the magnetic field in penumbrae. We again re-interprete the data of Hewagama et al. (1993), employing our spectral line synthesis for detailed analysis. The only direct method of measuring vertical field gradients is to employ data taken in two lines that are formed at different heights. Hewagama et al. (1993) compare magnetic field strengths from the Mg I 12.32 μm line with values from the Haleakala polarimeter measured in the Fe I 630.25 nm line. The two data sets may be compared, although they were taken a day apart, because the magnetic configuration changed only slowly. According to Mickey (private communication, 1993) the magnetic field vector **B** was derived from the Haleakala data using the inversion technique of Skumanich & Lites (1987),

Table 1. Magnetic field data from Hewagama et al. (1993, Figs. 8 and 9) and vertical field strength gradients derived from these. Magnetic field strengths B and inclinations γ measured from the Mg I 12.32 μm and Fe I 630.25 nm lines are specified as function of distance from spot center, in units of the penumbral radius R/R_P (first five columns). The remaining columns give, for three RE models, computed Stokes Q formation heights z per line and the corresponding field gradient $-\partial B/\partial z$ in G km^{-1}

					$T_{\rm eff}$ = 4500			$T_{\rm eff}$ = 5000			$T_{\rm eff}$ = 5500		
R/R_P	B_{Mg} [G]	B_{Fe} [G]	γ_{Mg}	γ_{Fe}	z_{Mg} [km]	z_{Fe} [km]	$-\partial B/\partial z$ [G km^{-1}]	z_{Mg} [km]	z_{Fe} [km]	$-\partial B/\partial z$ [G km^{-1}]	z_{Mg} [km]	z_{Fe} [km]	$-\partial B/\partial z$ [G km^{-1}]
−1.10	585	815	92	78	262	96	1.39	336	129	1.11	382	156	1.02
−0.87	765	1060	72	66	251	118	2.22	336	169	1.77	369	156	1.39
−0.73	885	1400	64	60	251	130	4.24	336	182	3.35	369	186	2.82
−0.58	1360	1725	50	55	240	163	4.74	336	209	2.87	369	201	2.18
0.59	1550	1815	59	55	240	152	3.00	336	209	2.08	369	201	1.58
0.81	1080	1300	60	62	251	130	1.81	336	195	1.57	369	186	1.21
1.11	765	900	73	78	251	107	0.94	336	142	0.70	369	171	0.68

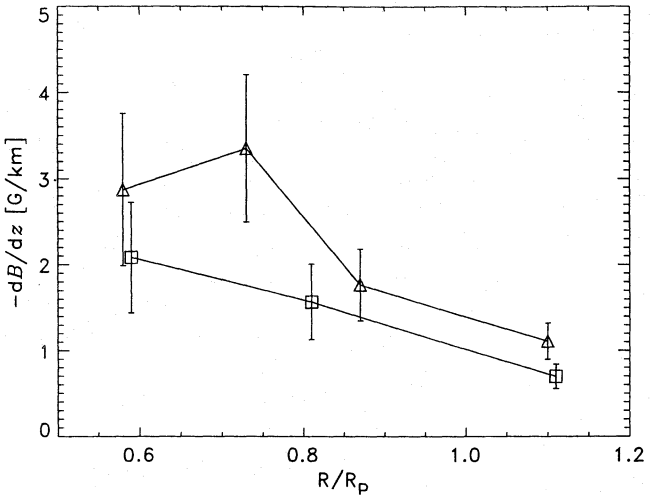

Fig. 10. Magnetic field gradients in the penumbra for RE model T5000. Points on different sides of the sunspot are marked by triangles and squares, respectively

which allows **B** to be measured with greater accuracy than most traditional methods do.

Since it is not clear which of our RE models is the more suitable here, and since large thermodynamical differences should exist between bright and dark penumbral fibrils, we have employed the three RE models with $T_{\rm eff}$ = 4500, 5000 and 5500 K to bracket the penumbral temperature range. In addition, the presence of penumbral inhomogeneity complicates the analysis. Both the 12.32 μm line and the Fe I 630.25 nm line measure an average of the magnetic field strength, vertically over about a scale height and horizontally over the size of the resolution element, which implies averaging over most of the small-scale inhomogeneity seen in high-resolution images of penumbrae.

The first thing to do is to determine formation heights of Mg I 12.32 μm and Fe I 630.25 nm, or rather, their response functions to magnetic fields. We use the peak of the line depression contribution function (Magain 1986; Grossmann-Doerth et al. 1988) as a crude measure of this response height. Since the contribution functions are strongly wavelength-dependent across the line profile, we have to choose a suitable wavelength; in addition, the different Stokes parameters need not have identical contribution functions. For the 12.32 μm line, which shows large Zeeman splitting at penumbral field strengths, we select the σ-peak wavelength as an obvious choice. Since the σ components are dominated by Stokes Q at field inclinations that are characteristic of penumbrae, we define the formation height as the height where the Stokes Q emission contribution function at that particular wavelength peaks. For the Fe I data the Stokes Q profiles also determine the derived formation heights of the magnetic signal, because these data were analysed using the Skumanich & Lites (1987) Stokes profile inversion method. We note, however, that using Stokes V peaks instead of Stokes Q produces no major changes in the results.

The magnetic field gradient then follows by dividing the measured field strength difference between the two lines by the computed difference in heights of formation. No interpolation between depth grid points has been applied in the determination of formation heights, because the grid spacing is much smaller than other uncertainties.

The first five columns of Table 1 present the magnetic field input data, while the remaining columns list the computed 12.32 μm and 630.25 nm line formation heights and the resulting field gradients for the T4500, T5000, and T5500 model atmospheres. The line contribution functions are not very sensitive to $T_{\rm eff}$, because the locations of the peaks of the contribution function at the wavelength of Stokes Q maximum do not vary much in terms of continuum optical depth (Fig. 5), while only slight differences result from the conversion of optical depth to physical height scales.

The gradients for the T5000 model are intermediate between the hotter and cooler models, so the T5000 results may be considered as characteristic for actual penumbral field gradients. They are also shown in Fig. 10. Their magnitude is similar to most estimates for the vertical field gradients in umbrae that have been obtained in similar fashion (Wittmann 1974: 1.0 ± 0.5 G km^{-1} at h = 700 km; Pahlke 1988: 2.0–2.5 G km^{-1}), but it exceeds most estimates that are based on

other techniques, such as combining transverse magnetic field measurements with imposing the $\nabla \cdot \mathbf{B} = 0$ condition (Hagyard et al. 1983: 0.1–0.4 G km^{-1}; Hofmann & Rendtel 1989: 0.32 G km^{-1}), and it also exceeds the 0.4–0.7 G km^{-1} values that result from theoretical sunspot modeling such as the self-similar model (Schlüter & Temesvary 1958; Osherovich 1980) and the return-flux model (Osherovich 1982; Flå et al. 1982; Osherovich 1984). For penumbrae, there is to our knowledge only the single analysis by Balthasar & Schmidt (1993), who find gradients of 2.5 – 3 G km^{-1} in the penumbra and outer parts of the umbra; the scarcity is presumably due to the limited accuracy of penumbral field measurements so far.

Apart from the gradient sizes, there are two other important results in Table 1 and Fig. 10. The first is the presence of systematic trends to larger gradients closer to the umbra, which is in agreement with the theoretical sunspot models cited above. We believe that these changes are real, independently of the correctness of the gradient sizes, because they are larger than the relative errors in the gradients, which are primarily due to uncertainties in the temperature behavior with $R/R_{\rm P}$. The second is the asymmetry between the two sides of the spot (displayed as difference between triangles and squares in Fig. 10). It may in part be due to the azimuthal averaging applied to the Fe I 630.25 nm data, but it may also be due to true sunspot asymmetry.

Are the large values of the vertical gradients found here realistic? They are affected by several uncertainties in the two-line analysis. The first is the measurement of the average field strength from each line. The Mg I 12 μm measurements should be quite accurate, because the emission peak is fully split and the σ-peak separation is directly proportional to the average field strength. The fitting procedure of Hewagama (1991) and Hewagama et al. (1993) also allows for σ-peak broadening due to inhomogeneities within the field of view; different σ and π widths are allowed for and both are fitted independently. The Fe I 630.25 nm field measurements rely on the line profile inversion method of Skumanich & Lites (1987), which has been demonstrated to produce reliable and reproduceable magnetic field values for a wide range of atmospheric parameters. It does give less accurate thermodynamic parameters from line profiles that are spatial averages over inhomogeneous fields (Lites & Skumanich 1990), but then produces an average value which should be well suited for comparison with the 12 μm results.

The computed difference in formation heights between the two lines is obviously model dependent. One uncertainty is the validity of hydrostatic equilibrium. The "chromospheric extension" derived by Deming et al. (1992) points to excess (over hydrostatic) density in the chromosphere, as do other eclipse observations (Lindsey et al. 1992, Belkora et al. 1992, Ewell Jr. et al. 1993), but not to discrepancies at the level of 12.32 μm line formation when observed at the disk, since the observations and modeling agree out to the limb (Carlsson et al. 1992a). The effects of photospheric dynamics on 12.32 μm profiles have been modeled by Rutten & Carlsson (1993) for the case of granulation, which produces only slight variations in the height of line formation. However, penumbral inhomogeneity probably causes larger departure from hydrostatic equilibrium and plane-parallel modeling in the upper penumbra photosphere than granulation causes in the quiet upper photosphere. The error bars in Fig. 10 are therefore sizable. They correspond to an error (plus and minus) equal to 0.25 dex in $\log \tau_{500}$ (approximately half a scale height); such variation may change the resulting field gradient by as much as 50%.

Notwithstanding these rather large uncertainties, we feel that this direct method of comparing data from two heights is more reliable than field extrapolations based on a potential-field assumption or the zero-divergence requirement of the magnetic field ($\nabla \cdot \mathbf{B} = 0$). Such indirect methods require the field to be rather smooth and homogeneous, whereas the penumbral field at photospheric heights consists at least of two major components: strongly inclined (nearly horizontal) fields and less inclined (more vertical) fields that merge alternatingly in a crossed-combs-like structure (e.g. Degenhardt & Wiehr 1991, Schmidt et al. 1992, Title et al. 1993). If also broad-band circular polarization is considered, it is found that the more horizontal component is restricted in height. The picture of the fine-scale penumbral field derived by Solanki & Montavon (1993) is that almost horizontal flux tubes, which carry the Evershed flow, are surrounded by inclined magnetic field which fills all the left-over space. Since the Evershed flow decreases in strength with height in the atmosphere, Solanki & Montavon (1993) propose that the number density of the horizontal flux tubes also decreases with height (cf. Degenhardt 1993). This leaves more space for the inclined field component to expand in; the net result is that there is a strong vertical gradient of the penumbral field strength while the averaged horizontal gradients are small. Thus, any method that relies on the averaged horizontal gradients to compute vertical gradients assuming divergence-free field fails to recognize that only the more vertical component of the field persists to large heights. Similar problems hold for potential field extrapolation, since it uses the average photospheric field as a boundary condition for extrapolation to larger height.

8. Canopy height in superpenumbrae

Magnetically split and polarized 12 μm line profiles are also observed outside visible sunspots (Deming et al. 1988; Hewagama et al. 1993). In the immediate vicinity of penumbrae, the emergent continuum intensity is unaffected by the magnetic field, but the lines indicate that the strength and direction of the magnetic field continue the trends present in the outer penumbra. In addition, the magnetic volume filling factor f drops steadily with increasing distance from the boundary of the visible sunspot. Hewagama (1991) and Hewagama et al. (1993) estimate a quantity which they call "degree of polarization" but which does not include depolarization by continuum processes. They determine it from fits to the measured Stokes vectors by assuming that the lines are optically thin and first subtracting a Gaussian absorption profile to remove the absorption trough from Stokes I. It is an indicator for the volume filling factor f of the magnetic field; we simply call it so henceforth. Their results should be rather reliably convertible into filling factor assuming that the temper-

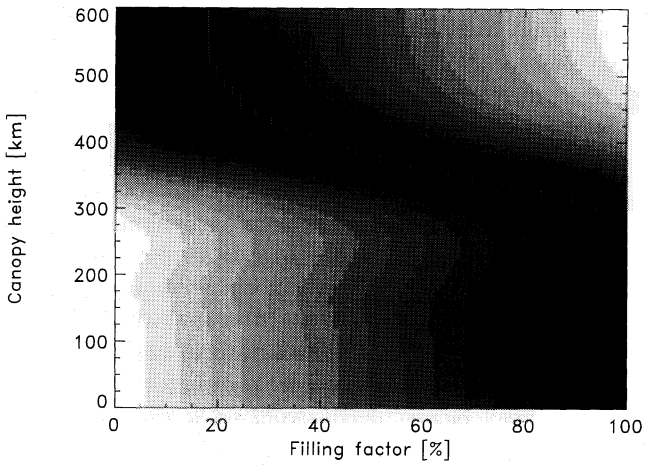

Fig. 11. Integrated absolute intensity differences between profiles from atmospheres with different magnetic filling factors f ranging from $f = 0\%$ to $f = 100\%$ (abscissa) and profiles from atmospheres with different canopy base heights h_c ranging from $h_c = 0$ km to $h_c = 600$ km (ordinate). All field is horizontal, with $B = 500$ G. Dark signifies small difference. The slanted dark band represents the most probable conversion factor between apparent filling factor and actual canopy base height

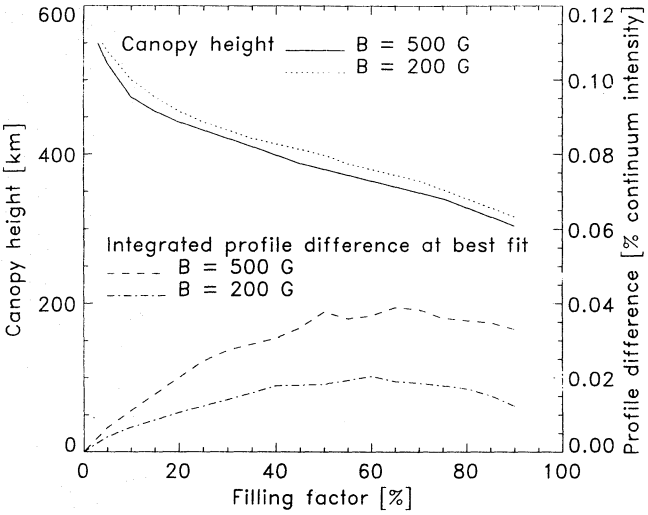

Fig. 12. *Upper part:* best-fit canopy height h_c vs. magnetic filling factor f relations for magnetic field strengths $B = 500$ and 200 G (lefthand ordinate scale). No relations are shown for the smallest and largest f where they are uncertain (large spread in Fig. 11). *Lower part:* the minimum difference between line profiles for different h_c and for the filling factor f, expressed as the average intensity difference over the line profile in percent of the continuum intensity (righthand ordinate scale)

ature in the superpenumbral magnetic features is the same as in the non-magnetic surroundings, because, in the penumbral and quiet-Sun temperature range, the emission peak strength is near its maximum and does not vary strongly with temperature (cf. Figs. 4 – 3). Hewagama et al. (1993) find that the magnetic filling factor at the height of Mg I 12 μm line formation exceeds 50% out to about 1.8 penumbral radii. Their field of view was rather large (a circular aperture of 4.5″ diameter, i.e. about a third of the projected penumbral radius), so that considerable averaging must have taken place over actual spatial variations of the magnetic filling factor and field strength.

It is well known that sunspots are surrounded by a magnetic "canopy" (filling factor 100%) that overlies non-magnetic photosphere in which magnetic fields are arranged in small discrete elements (e.g. Giovanelli 1980; Giovanelli & Jones 1982; Solanki et al. 1992, 1994). The base of the canopy lies in the upper photosphere and rises upwards outward. Its height h_c affects the strength of the polarized Stokes parameters of the 12 μm lines sensitively, because these originate from layers at about $h = h_c$; the canopy height therefore strongly influences the apparent magnetic filling factor obtained from these lines. Thus, we suspect that what is measured as "degree of polarization" or apparent volume filling factor by Hewagama et al. (1993) actually pertains to changes in canopy properties, especially canopy base height.

We first use Mg I 12.32 μm line computations to derive a conversion from apparent filling factor to canopy base height, assuming constant field strengths (but finding that the conversion does not depend sensitively on field strength). We take horizontal fields of two different strengths which are consistent with the measurements of Hewagama et al. (1993) in the vicin-

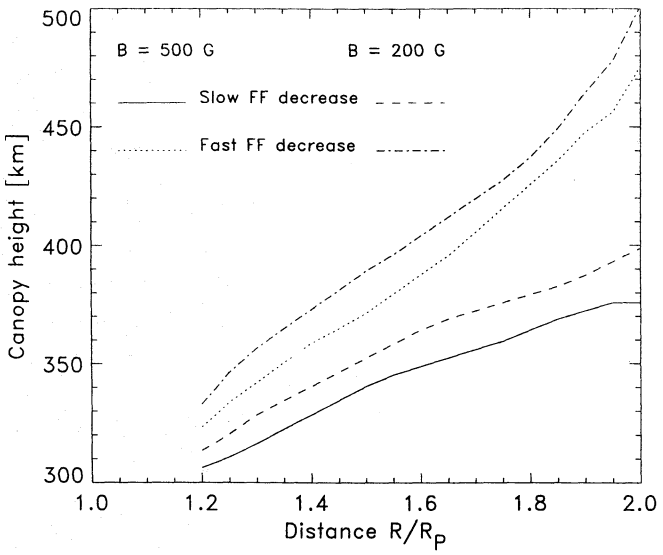

Fig. 13. Superpenumbral canopy height as function of distance R/R_P from spot center, for two cases of outward filling factor decrease, respectively 50% (slow) and 90% (fast) per unit R/R_P outside the penumbral radius R_P, and two constant magnetic field strengths, respectively 200 and 500 G. The upper curves are a better estimate of actual canopy behavior if there are also non-sunspot magnetic fluxtubes in the field of view, as is probably the case

ity of a penumbra, a value of 500 G representing the edge of the penumbra (at radius $R/R_P = 1$ from spot center) and a value of 200 G representing the field at about $R/R_P = 2$. We employ RE model T5750 because the atmospheric parameters should be representative of the quiet Sun; we neglect the influence of the magnetic field on the atmosphere. A comparison is then made between two series of Mg I 12 μm Stokes I profiles: one series computed from atmospheres in which horizontal magnetic fields are present only above a given canopy height, the other series computed from two-component atmospheres which contain horizontal magnetic fields down to the deep photosphere only above a surface fraction f, and non-magnetic plasma for the remaining fraction $(1 - f)$ of the volume. The first series of profiles is computed for a range of canopy base heights h_c; the second for a range of filling factors f. We then evaluate differences between the 12.32 μm profiles for every combination from the two series by integrating their Stokes I intensity difference profile over the spectral line width. At a given photospheric filling factor f, we now define the canopy height to be that one for which the integrated difference between the corresponding line profiles is minimal. Care has been taken that not only the integrated intensity difference be minimal, but that there are also no overly large point-to-point differences between the profiles.

Results are shown in Figs. 11–12. Figure 11 displays the behavior of the integrated profile differences as function of canopy height and filling factor, in the case of horizontal fields with $B = 500$ G independent of R/R_P. For filling factors $20\% \leq f \leq 80\%$ the best-fit canopy height is defined with good accuracy (± 20 km in the absence of systematic errors), while for $f \approx 0$ and $f \approx 100\%$ only lower and upper limits can be set, respectively. In the latter domains the canopy height no longer resides within the formation region of the Mg I 12 μm lines.

Figure 12 shows the resulting best-fit h_c–f relations for the two magnetic field values $B = 200$ G and $B = 500$ G. They differ only slightly, indicating that there is not much sensitivity to the field strength decay over the range $R/R_P = 1 - 2$. The lower part of the figure shows the integrated profile differences that correspond to the best-fit relations (righthand ordinate). The largest point-to-point intensity differences are generally an order of magnitude larger, but they remain much smaller than the size of the emission peaks.

These computations indicate that the apparent filling factors found by Hewagama et al. (1993) may be re-interpreted as canopy base heights $h_c = 300$–500 km above $\tau_{500} = 1$ just outside penumbrae, with a slight decrease for increasing apparent filling factor. The next step is to use these calibrations to determine h_c as a function of distance R/R_P from the outer penumbral edge. We use the data in Fig. 10 of Hewagama et al. (1993), which plots "degree of polarization" (apparent magnetic filling factor) against R/R_P. Since the scatter in this figure probably does not reflect variations in h_c, we refrain from determining h_c for each individual data point but instead set limits on h_c by defining upper and lower envelopes to the data points in the figure. These envelopes are wedge-shaped; they start both at $R/R_P = 1$ and $f = 100\%$, and have linear outward decreases of Δf of 50% and of 90% per unit R/R_P, respectively. Figure 13 shows the results of converting these envelopes into canopy height h_c by means of Fig. 12, neglecting the dependence of h_c on B because it only increases the total variation by 20–30 km over $R/R_P = 1.2 - 2$. The upper envelope is marked as slow filling-factor decrease, the lower envelope as fast filling-factor decrease. The mean of the four curves indicates an increase of canopy base height from about $h_c = 320$ km to about $h_c = 420$ km over $R/R_P = 1.2 - 2$. This result corresponds very well with the canopy base height increase that is derived from the Fe I lines at 1.5 μm by Solanki et al. (1992, 1994). Their result lies between the dashed and dotted curves in Fig. 13 over $R/R_P = 1.3 - 1.7$.

We suspect that much of the uncertainty in the h_c relations in Fig. 13, i.e. much of the scatter in the data in Fig. 10 of Hewagama et al. (1993), results from lack of distinction between the superpenumbral canopy and the presence of small magnetic elements with large field strength ("fluxtubes") in the underlying photosphere. The latter expand with height, so that both types of magnetic structure reach about the same field strength in the upper photosphere; the 12.32 μm line probably does not discriminate between them. In contrast, with Fe I 1.5 μm profiles one can readily distinguish between these different types of feature; the presence of small magnetic elements below the canopy has been clearly demonstrated by Solanki et al. (1992). Such non-sunspot magnetic elements will add to the apparent filling factor determined from the 12.32 μm line; thus, our lower envelope to the data points of Hewagama et al. (1993), which produces the upper curves in Fig. 13, is probably a better estimator of the canopy base height h_c than the upper envelope; the latter (lower curves in Fig. 13) provides only a lower limit to h_c.

The above re-interpretation of "degree of polarization" as canopy base height is supported by noting that a correlation exists between apparent filling factor and magnetic field inclination. When one compares Figs. 6 and 10 of Hewagama et al. (1993), a tendency emerges for the field to be more vertical at a given R/R_P for those data points that correspond to larger apparent filling factor. Since the superpenumbral canopy field is nearly horizontal whereas that of fluxtube-like magnetic elements is still mostly vertical at 12 μm formation heights, one would indeed expect such correlation if part of the scatter is due to contamination by non-sunspot magnetic elements.

9. Conclusion

We have systematically synthesized and analysed the Mg I 12.32 μm emission line in the presence of magnetic fields. We first used test computations to study the formation of the 12.32 μm line. We found that the overall behavior of the emission peak in non-magnetic areas, penumbrae and umbrae follows simply from Saha-Boltzmann population statistics, and that the Stokes V profile is completely split already for $B \geq 200$ G at solar photospheric temperatures, and for a slightly higher value of B at lower temperatures. Our tests suggest that

even relatively simple fits to observed profiles should return rather accurate B and γ values.

In addition to these test computations, we have modeled observed features of the 12.32 μm line from sunspots. We have concentrated on three observations:

1. *The excess width of the σ components relative to the π component.* This excess is, if at all, only partly due to vertical gradients in field strength. The smooth radial variaton present across penumbrae is a more important source and probably the dominant one. Integrated over the field of view, it produces just about the observed excess broadening. Additional broadening by horizontal small-scale field variations is constrained to variations ΔB below about ± 200 G.
2. *Vertical magnetic field gradients in the penumbra.* From the observed difference between the magnetic splitting of the Mg I 12.32 μm line and the Fe I 630.25 nm line we have derived the vertical field strength gradient $\partial B/\partial z$ in the penumbra. It varies between $\partial B/\partial z = 0.7\,\mathrm{G\,km^{-1}}$ at the outer boundary of the penumbra and $\partial B/\partial z = 3.0\,\mathrm{G\,km^{-1}}$ near the umbra.
3. *Superpenumbral magnetic fields.* Finally, we have reinterpreted the observation of the large "degree of polarization" just outside a sunspot (Hewagama et al. 1993) as the result of horizontal field in a superpenumbral magnetic canopy. The base height of this canopy is found to lie in the upper photosphere, in excellent agreement with observations taken at 1.5 μm. Due to its greater formation height, the 12.32 μm line shows a much stronger signal from the canopy field. We use this property to estimate the canopy geometry (Fig. 13).

In summary, by modeling the Mg I 12.32 μm emission line in detail we have apppreciably extended the diagnostic merits of this line for the investigation of penumbral and superpenumbral magnetic fields near the temperature minimum. The value of further modeling will depend on the quality of future data. For example, measurements with higher spatial resolution than available at present will help to set tighter limits on small-scale penumbral field variations. A better signal-to-noise ratio may solve the remaining issue of the amplitude differences between 12.32 μm σ peaks.

Acknowledgements. We thank R.L. Kurucz for providing line-blanketed radiative equilibrium models, D. Mickey for providing details about the Haleakala Stokes profile analysis, and D. Deming for clarifying some points regarding the 12 μm observations. R.J. Rutten acknowledges a Fulbright scholarship administered by the Netherlands America Commission for Educational Exchange and the hospitality of the National Solar Observatory/Sacramento Peak.

References

Anderson L., 1991, in L. Crivellari, I. Hubeny, D. G. Hummer (eds.), Stellar Atmospheres: Beyond Classical Models, NATO ASI Series C-341, KLuwer, Dordrecht, p. 29
Anderson L. S., 1985, ApJ 298, 848
Anderson L. S., 1989, ApJ 339, 558
Auer L. H., Heasley J. N., 1978, ApJ 64, 67
Auer L. H., Heasley J. N., Milkey R. W., 1972, A Computational Method for the Solution of Non-LTE Transfer Problems by the Complete Linearization Method, Contribution No. 555, Kitt Peak National Observatory
Avrett E. H., Chang E. S., Loeser R., 1993, in D. Rabin, J. Jefferies, C. A. Lindsey (eds.), Infrared Solar Physics, Proc. Symp. 154 IAU (Tucson), Kluwer, Dordrecht, p. 323
Balthasar H., Schmidt W., 1993, A&A 279, 243
Belkora L., Hurford G. J., Gary D. E., Woody D. P., 1992, ApJ 400, 692
Brault J., Noyes R., 1983, ApJ 269, L61
Bruls J. H. M. J., 1992, Formation of diagnostic lines in the solar spectrum, PhD Thesis, Rijksuniversiteit Utrecht, Utrecht
Canfield R. C., Cram L. E., 1977, ApJ 216, 654
Canfield R. C., Pasachoff J. M., Stencel R. E., Beckers J. M., 1978, Solar Phys. 58, 263
Carlsson M., 1986, A Computer Program for Solving Multi-Level Non-LTE Radiative Transfer Problems in Moving or Static Atmospheres, Report No. 33, Uppsala Astronomical Observatory
Carlsson M., Rutten R. J., 1992, A&A 259, L53
Carlsson M., Rutten R. J., 1993, in D. R. Rabin, J. T. Jefferies, C. A. Lindsey (eds.), Infrared Solar Physics, Proc. Symp. 154 IAU (Tucson), Kluwer, Dordrecht, p. 341
Carlsson M., Rutten R. J., Shchukina N. G., 1990, in L. Deszö (ed.), The Dynamic Sun, Proc. EPS 6^{th} European Solar Meeting, Publ. Debrecen Heliophysical Observatory **7**, Debrecen, p. 260
Carlsson M., Rutten R. J., Shchukina N. G., 1992a, A&A 253, 567
Carlsson M., Rutten R. J., Shchukina N. G., 1992b, in M. S. Giampapa, J. A. Bookbinder (eds.), Cool Stars, Stellar Systems, and the Sun, Proc. Seventh Cambridge Workshop, Astron. Soc. Pac. Conf. Series 26, p. 518
Chang E. S., 1987, Physica Scripta 35, 792
Chang E. S., Avrett E. H., Mauas P. J., Noyes R. W., Loeser R., 1991, ApJ 379, L79
Degenhardt D., 1993, A&A 277, 235
Degenhardt D., Wiehr E., 1991, A&A 252, 821
Deming D., Boyle R. J., Jennings D. E., Wiedemann G., 1988, ApJ 333, 978
Deming D., Jennings D., Jefferies J., Lindsey C., 1991, in A. N. Cox, W. C. Livingston, M. S. Matthews (eds.), Solar interior and atmosphere, University of Arizona Press, Tucson, p. 933
Deming D., Jennings D. E., McCabe G., Noyes R., Wiedemann G., Espenak F., 1992, ApJ 396, L53
Edvardsson B., Andersen J., Gustafsson B., Lambert D. L., Nissen P. E., Tomkin J., 1993, A&A 275, 101
Ewell Jr. M. W., Zirin H., Jensen J. B., 1993, ApJ 403, 426
Flå T., Osherovich V. A., Skumanich A., 1982, ApJ 261, 700
Giovanelli R. G., 1980, Solar Phys. 68, 49
Giovanelli R. G., Jones H. P., 1982, Solar Phys. 79, 267
Grossmann-Doerth U., Larsson B., Solanki S. K., 1988, A&A 204, 266
Hagyard M. J., Teuber D., West E. A., Tandberg-Hanssen E., Henze W., Beckers J. M., Bruner M., Hyder C. L., Woodgate B. E., 1983, Solar Phys. 84, 13
Hewagama T., 1991, An infrared polarimetric study of sunspots, Ph.D. Thesis, University of Maryland, College Park, Maryland
Hewagama T., Deming D., Jennings D. E., Osherovich V., Wiedemann G., Zipoy D., Mickey D. L., Garcia H., 1993, ApJS 86, 313
Hofmann A., Rendtel J., 1989, Astron. Nachr. 310, 61
Illing R. M. E., Landman D. A., Mickey D. L., 1975, A&A 41, 183
Jahn K., 1989, A&A 222, 264

Kurucz R. L., 1991, in L. Crivellari, I. Hubeny, D. G. Hummer (eds.), Stellar Atmospheres: Beyond Classical Models, NATO ASI Series C-341, Kluwer, Dordrecht, p. 441
Lemke M., Holweger H., 1987, A&A 173, 375
Lemoine B., Demuynck C., Destombes J. L., 1988, A&A 191, L4
Lindsey C., Clark T. A., Harrison R. A., Carter M. K., Watt G., Becklin E. E., Roellig T. L., Braun D. C., Naylor D. A., Tompkins G. J., 1992, Nat 358, 6384
Lites B. W., Scharmer G. B., Skumanich A., 1990, ApJ 355, 329
Lites B. W., Skumanich A., 1990, ApJ 348, 747
Magain P., 1986, A&A 163, 135
Makita M., 1986, Solar Phys. 106, 269
Mathisen R., 1984, Oslo Inst. Theor. Astrophys. Publ. Series 1, 1
Mathys G., 1990, A&A 232, 151
Murphy G. A., 1990, The Synthesis and Inversion of Stokes Spectral Profiles, NCAR Cooperative Thesis No. 124, High Altitude Observatory, Boulder
Murphy G. A., Rees D. E., 1990, Operation of the Stokes Profile Synthesis Routine, NCAR Technical Note NCAR/TN-348+IA, High Altitude Observatory, Boulder
Olson G. L., Auer L. H., Buchler J. R., 1986, J. Quant. Spectrosc. Radiat. Transfer 35, 431
Osherovich V., 1980, Solar Phys. 68, 297
Osherovich V., 1982, Solar Phys. 77, 63
Osherovich V., 1984, Solar Phys. 90, 31
Pahlke K.-D., 1988, Analyse von Feinstrukturen in Sonnenflecken-Umbren aus Stokes-V Messungen, PhD Thesis, Göttingen University
Pizzo V. J., 1986, ApJ 302, 785
Rees D. E., 1969, Solar Phys. 10, 268
Rees D. E., 1987, in W. Kalkofen (ed.), Numerical Radiative Transfer, Cambridge University Press, Cambridge, Great Britain, p. 213
Rees D. E., Murphy G. A., Durrant C. J., 1989, ApJ 339, 1093
Rutten R. J., Carlsson M., 1993, in D. R. Rabin, J. T. Jefferies, C. A. Lindsey (eds.), Infrared Solar Physics, Proc. Symp. 154 IAU (Tucson), Kluwer, Dordrecht, p. 309
Sánchez Almeida J., Lites B. W., 1992, ApJ 398, 359
Schlüter A., Temesvary S., 1958, in D. Lehnert (ed.), Electromagnetic Phenomena in Cosmical Physics, Proc. IAU Symp. 6, 263
Schmidt W., Hoffmann A., Balthasar H., Tarbell T., Frank Z., 1992, A&A 264, L27
Seares F. H., 1913, ApJ 38, 99
Skumanich A., Lites B. W., 1987, ApJ 322, 473
Solanki S. K., 1993, in D. M. Rabin, J. T. Jefferies (eds.), Infrared Solar Physics, Proc. Symp. 154 IAU (Tucson), Kluwer, Dordrecht, p. 393
Solanki S. K., Montavon C. A. P., 1993, A&A 275, 283
Solanki S. K., Pahlke K. D., 1988, A&A 201, 143
Solanki S. K., Rüedi I., Livingston W., 1992, A&A 263, 339
Solanki S. K., Montavon C. A. P., Livingston W., 1994, A&A 283, 221
Title A. M., Frank Z. A., Shine R. A., Tarbell T. D., Topka K. P., Scharmer G., Schmidt W., 1993, ApJ 403, 780
Wijbenga J. W., Zwaan C., 1972, Solar Phys. 23, 265
Wittmann A., 1974, Solar Phys. 36, 29
Zirin H., Popp B., 1989, ApJ 340, 571

This article was processed by the author using Springer-Verlag LaTeX A&A style file version 3.